energies

Article

A Self-Supplied Power Optimizer for Piezoelectric Energy Harvesters Operating under Non-Sinusoidal Vibrations

Luigi Costanzo *, Alessandro Lo Schiavo and Massimo Vitelli

Department of Engineering, Università degli Studi della Campania "Luigi Vanvitelli", 81031 Aversa, Italy; alessandro.loschiavo@unicampania.it (A.L.S.); massimo.vitelli@unicampania.it (M.V.)
* Correspondence: luigi.costanzo@unicampania.it

Abstract: A self-supplied circuit that is able to significantly increase the power delivered to a bridge rectifier by a Resonant Piezoelectric Vibration Energy Harvester (RPVEH) is presented and discussed. The proposed circuit, called the Energy Harvester Power Optimizer (EHPO), is implemented by means of a switch-mode converter that emulates a negative capacitance. Unlike switch-mode impedance emulators, based on sophisticated tracking algorithms requiring lossy microcontrollers, EHPO exploits a very light control circuit based on a hysteresis comparator. The EHPO is self-supplied since it does not need an external supply, but it draws the energy for its operation directly from the RPVEH. Moreover, it is developed without the assumption of purely sinusoidal vibrations. Experimental results show that the EHPO can significantly increase the power delivered to a rectifier, both in the case of sinusoidal vibrations (percent gain of the net extracted power up to about 190%) and non-sinusoidal vibrations (percent gain of the net extracted power up to about 245%), regardless of the shape of the forcing acceleration and regardless of the RPVEH resonance frequency.

Keywords: piezoelectric vibration energy harvesters; non-sinusoidal vibrations; power optimization

check for updates

Citation: Costanzo, L.; Lo Schiavo, A.; Vitelli, M. A Self-Supplied Power Optimizer for Piezoelectric Energy Harvesters Operating under Non-Sinusoidal Vibrations. *Energies* **2023**, *16*, 4368. https://doi.org/10.3390/en16114368

Academic Editor: Javier Contreras

Received: 24 April 2023
Revised: 24 May 2023
Accepted: 24 May 2023
Published: 27 May 2023

1. Introduction

Most wireless sensor networks are fed by standard primary batteries or rechargeable batteries [1–3]. Batteries have many drawbacks, such as their high cost, limited reliability, need for frequent maintenance (recharge or replacement), and risk to the environment due to hazardous chemical materials. Energy harvesting offers an alternative to battery replacement or, at least, an increase in their lifetime [4–6]. The last few years have seen increasing attention devoted to Resonant Piezoelectric Vibration Energy Harvesters (RPVEHs). Recent developments have concerned both the harvester electronic interfaces, aimed at increasing the extracted power [7,8], and the piezoelectric material properties, which contribute to the harvesting performance [9,10]. Significant attention has also been devoted to magnetically activated piezoelectric composites for their promising potential in IoT applications [11,12].

In the presence of sinusoidal vibrations with an angular frequency ω, the load impedance $Z_{OPT}(j\omega)$ that maximizes the average power transferred from a harvester to a linear load must be equal to the complex conjugate of the equivalent RPVEH internal impedance $Z_{eq}(j\omega)$ [13]. However, in practical applications, the output voltage of an RPVEH needs to be rectified using an AC/DC converter that should be able to emulate $Z_{OPT}(j\omega)$ [7]. Since ω (and hence also Z_{OPT}) can vary over time, it is also necessary to carry out a tracking process to dynamically emulate the optimal impedance in any possible operating condition. Several single or double-stage active AC/DC converters have been proposed in the literature aimed at the emulation of Z_{OPT} [8–17]. However, they cannot be self-supplied due to the complexity of their power stage and their control techniques, usually implemented through lossy microcontrollers. This is the main reason why, in most cases, a passive bridge rectifier is employed for the rectification of the RPVEH output voltage. To the best of the authors' knowledge, nearly all of the commercial power electronics boards, available on the market for piezoelectric energy-harvesting applications, are equipped with a passive bridge rectifier [18–21]. Unfortunately, in many cases, passive bridge rectifiers cannot extract the maximum power from RPVEHs, since they are not able to emulate Z_{OPT} [7]. Therefore, the performance of RPVEHs connected to passive bridge rectifiers can be further improved, even if they are equipped with Maximum Power Point Tracking controllers on their DC side [22]. To achieve that purpose, an inductor could be added, but the necessary value of the inductance is typically too large and cannot adapt to the variations of the input vibrations. As an alternative, interesting non-linear approaches, such as the SSHI [23,24] and the SECE techniques [25,26], have been developed.

In the case of non-sinusoidal vibrations, which are typically encountered in practical applications, it is not possible to define an optimal impedance $Z_{OPT}(j\omega)$. Instead, as it will be detailed in the following section, the time-domain compensation of the current $i_c(t)$ drawn by the RPVEH output capacitance C_{pz} can have a boost effect on the power extraction. In this paper, a new approach to compensate the current $i_c(t)$ is presented and discussed for the first time after patent granting [27]. The compensation of $i_c(t)$ is achieved by exploiting a self-supplied switch-mode converter with a light control that, in the following, will be called the "Energy Harvester Power Optimizer" (EHPO). The main characteristic of the EHPO is its capability to behave like a negative capacitance that efficiently operates under arbitrary vibration conditions [28,29]. The EHPO does not require a complex and lossy microcontroller because it does not implement a sophisticated control algorithm. The control circuit is as simple as those employed by SSHI and SECE circuits, and it is specifically designed for non-sinusoidal vibrations. Finally, the EHPO emulates the desired negative capacitance without using a linear amplifier, unlike the circuits that have been very effectively employed for the active damping of structures with piezoelectric transducers [28]. Such circuits provide reactive power to the transducer at the expense of their power supply and, hence, they are not energetically efficient for energy-harvesting applications.

The rest of the paper is organized as follows: In Section 2, the operating principle and the architecture of the EHPO are presented. In Section 3, the actual implementation and the relationships that are useful for design purposes are discussed. Finally, the experimental results are reported in Section 4. Our conclusions end the paper.

2. Operating Principle of the EHPO

The most used equivalent electric circuit of an RPVEH in a cantilever configuration is shown in Figure 1. m denotes the vibrating mass, k the equivalent stiffness of the piezoelectric cantilever, c the viscous damping coefficient, and θ the force factor describing the piezoelectric effect. Moreover, $\ddot{y}(t)$ is the clamp acceleration and $\dot{x}(t)$ is the speed of the cantilever tip. As shown in Figure 1, C_{pz} is the output capacitance of the piezo layers and $i_{pz}(t) = \theta \cdot \dot{x}(t)$ is the current generated by the piezoelectric effect, which is not only a function of time but also of the piezo output voltage, $v_{AB}(t)$.

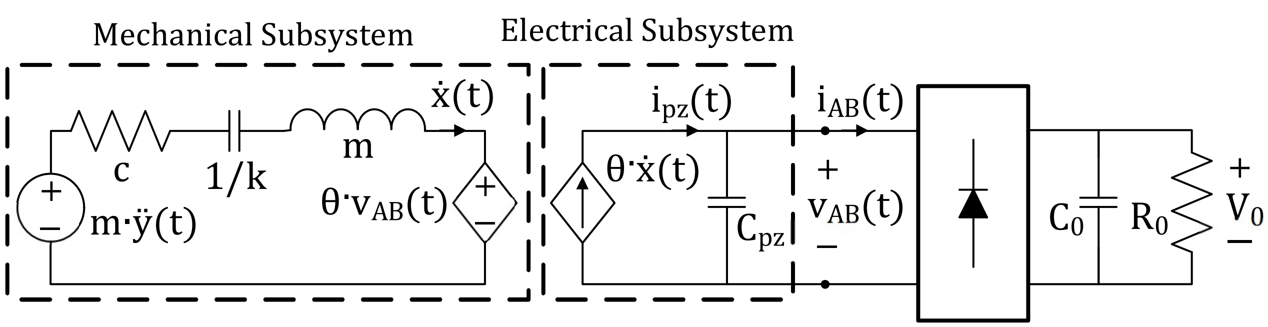

Figure 1. Equivalent electric circuit of an RPVEH loaded by a diode bridge rectifier.

The capacitance C_{pz} in the electrical subsystem of an RPVEH plays a negative effect on the extraction of power, significantly reducing the maximum power that the rectifier can extract from the harvester. Let us clarify such an aspect by assuming, for the sake of simplicity, negligible voltage drops across the diodes of the bridge rectifier in Figure 1 and $C_0 \gg C_{pz}$.

According to the typical current and voltage waveforms shown in Figure 2, when $i_{pz}(t) > 0$ ($i_{pz}(t) < 0$) and $v_{AB}(t) = V_0$ ($v_{AB} = -V_0$), it is $i_{AB}(t) = i_{pz}(t)$ leading to a power transfer, through the bridge rectifier, to the DC load. When $i_{pz}(t) > 0$ ($i_{pz}(t) < 0$) and $|v_{AB}(t)| < V_0$, it is $i_{AB}(t) = 0$, since $i_{pz}(t)$ flows inside C_{pz}. Hence, no instantaneous power can be transferred to the DC load. The capacitance C_{pz} draws the piezoelectric output current during the transitions of $v_{AB}(t)$ between the voltage limits $-V_0$ and $+V_0$ (from $-V_0$ to $+V_0$ and vice versa). The bigger C_{pz}, the longer the transitions delay. In order to maximize the power transferred to the load, it is necessary to minimize the time intervals when $|v_{AB}(t)| < V_0$ (and hence $i_{AB}(t) = 0$), that is, the rising and falling times of $v_{AB}(t)$ between $-V_0$ and $+V_0$.

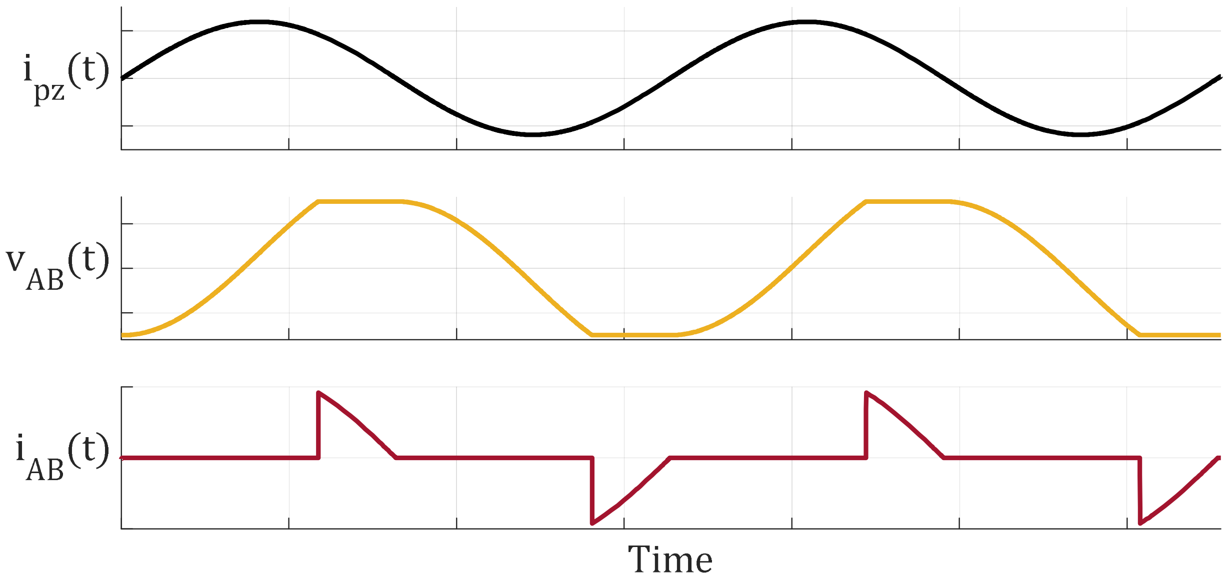

Figure 2. Typical current and voltage waveforms for a piezoelectric harvester loaded by a bridge rectifier, as shown in Figure 1.

In this paper, a self-supplied circuit to be connected in parallel to the bridge rectifier, EHPO, is proposed, as shown in Figure 3a. The target of the EHPO is to cancel the negative effect of C_{pz} by drawing a current $i_{EHPO}(t)$ equal to $-i_c(t)$, where $i_c(t)$ is the current drawn by C_{pz}. Thereby, the time intervals when $|v_{AB}(t)| < V_0$ are minimized and the power extraction is maximized. It should be highlighted that the EHPO is able to emulate the negative capacitance $-C_{pz}$ regardless of the shape of $v_{AB}(t)$ and without requiring an external supply. The EHPO is intended to draw $-i_c(t)$ whatever the working frequency and whatever the shape of the vibration waveform (sinusoidal or not). Such a property makes it incredibly more attractive from a practical point of view, with respect to all those techniques requiring tuning at a specific frequency [7].

The EHPO architecture is based on a switch-mode power converter whose input current is controlled as desired. As shown in the EHPO block diagram of Figure 3b, the input current is controlled by a feedback loop that ensures that $i_{EHPO}(t)$ follows the desired reference current $i_{ref}(t) = -i_c(t)$. Such a reference current, obtained by sensing the input voltage $v_{AB}(t)$, is the current that would be drawn by the desired negative capacitance $-C_{pz}$. Finally, the current control is implemented through a hysteretic controller, instead of the usual PWM controller, to obtain a faster response in non-sinusoidal reference tracking and to reduce the switching losses. Indeed, the hysteretic controller ensures the lowest switching frequency for a given tracking error.

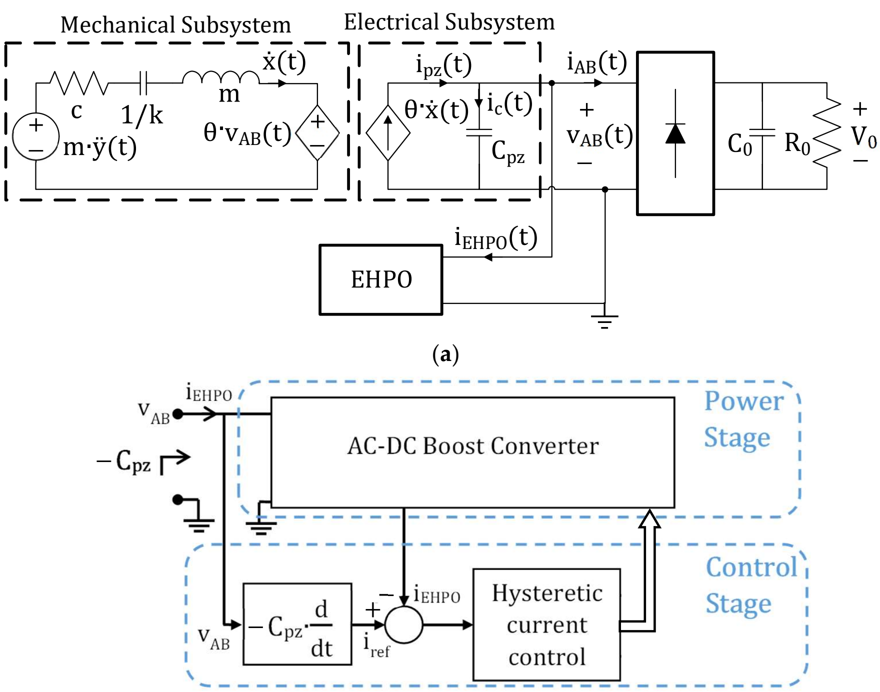

(a)

(b)

Figure 3. (a) Connection of EHPO in parallel between an RPVEH and a passive rectifier. (b) Block diagram of EHPO.

3. Design and Implementation of the EHPO

In this section, the circuit that implements the EHPO is presented, and its main characteristics are analyzed. Since the EHPO should emulate a negative capacitance, it must allow a bidirectional energy flow. Thus, as shown in Figure 4, it exploits an AC-DC boost converter based on a half-bridge topology, which allows a four-quadrant operation. The implementation of the feedback control loop is described in detail in the following section, and its simplicity, which avoids the adoption of an energy-hungry microcontroller, is shown. Next, the expected duty cycle and the switching frequency are evaluated as a function of the circuit parameters, as needed in the design phase.

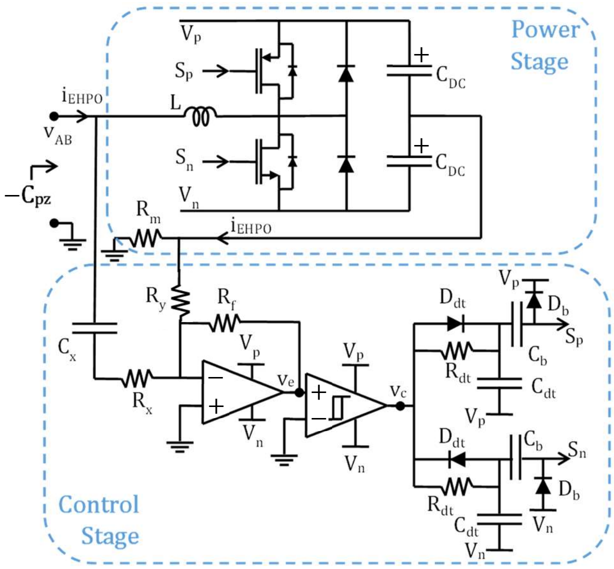

Figure 4. Schematic of EHPO.

3.1. The Feedback Control Loop

The negative capacitance block and the difference node, shown in the feedback loop of Figure 3b, are implemented by means of an operational amplifier circuit, as shown in Figure 4. Moreover, for the implementation of the hysteretic current control, a hysteresis comparator and two delay networks are used. The expression of the comparator input i.e., the voltage v_e, can be calculated by applying the Kirchhoff's current law to the op-amp inverting node. Under the assumption of $R_y \gg R_m$, it results in

$$v_e = -\frac{s \cdot R_f C_x}{1 + s \cdot R_x C_x} \cdot v_{AB} - \frac{R_f R_m}{R_y} \cdot i_{EHPO}, \tag{1}$$

which can be rewritten as

$$v_e = \frac{R_f R_m}{R_y}\left(i_{ref} - i_{EHPO}\right), \tag{2}$$

where

$$i_{ref} = -\frac{s \cdot R_y C_x}{R_m} \frac{1}{1 + s \cdot R_x C_x} \cdot v_{AB}. \tag{3}$$

It should be highlighted that the pole in Equation (3), due to the presence of R_x, is deliberately introduced to limit the op-amp gain at high frequencies and, thus, to prevent possible instability problems. However, if $1/(R_x C_x)$ is sufficiently higher than the angular frequency band ω of the input voltage v_{AB} i.e., $\omega \ll 1/(R_x C_x)$, Equation (3) can be simplified as

$$i_{ref} = -\frac{s \cdot R_y C_x}{R_m} \cdot v_{AB}. \tag{4}$$

Equations (2) and (4) confirm that the operational amplifier implements the difference block shown in Figure 3b and that the reference current is proportional to the opposite of the derivative of the input voltage v_{AB}.

The negative feedback loop keeps the comparator input v_e within a hysteresis band ΔV_H around zero. If the hysteresis band is sufficiently small, it is $v_e \cong 0$ and, according to Equations (2) and (4), it results in

$$i_{EHPO} = -s \cdot \frac{C_x R_y}{R_m} \cdot v_{AB}. \tag{5}$$

Equation (5) proves that, under current control, the EHPO draws a current that is proportional to the opposite of the time derivative of $v_{AB}(t)$, that is, the EHPO emulates a negative capacitance. The emulated negative capacitance is just equal to $-C_{pz}$ provided that $C_x R_y / R_m = C_{pz}$. Therefore, the values of the resistances R_y and R_m and of the capacitance C_x should be chosen according to the value of the internal capacitance C_{pz} of the specific piezoelectric harvester to be compensated. However, such values are independent of the shape of the input vibrations and the possible mechanical tuning of the cantilever structure of the RPVEH, which regulates its resonance frequency [5].

Note that, a dead time is introduced in the control signals (S_p and S_n) of the upper and lower MOS switches of the converter leg, by means of the two delay networks made up by R_{dt}, C_{dt}, and D_{dt} at the output of the hysteresis comparator. This is enacted to prevent the simultaneous conduction of the two MOS in correspondence with the commutation times. In this way, the turn-on of a MOS is delayed by the $R_{dt}C_{dt}$ network and the turn-off of the other MOS is sped up by the action of diode D_{dt}. Moreover, the presence of the two networks composed by C_b and D_b ensures that none of the two MOS switches remain blocked in the ON state at the system start-up, when the capacitors C_{DC} are not still charged. In particular, the capacitor C_b is large enough to behave like a short circuit in normal operations, whereas, to avoid the MOS remaining blocked in the ON state, it disconnects its gate from the relative control signal after a sufficiently long stationary time. In this way, the reverse current of the diode D_b turns off the MOS.

It is worth noting that, with reference to the hysteretic controller, the amplitude of the hysteresis band of the comparator determines the acceptable error on the voltage tracking. Such an error, as will be investigated in the next section, is also affected by the delay introduced by the comparator. Due to the low power constraints of the considered application, the chosen comparator should have a very low power consumption, which unavoidably leads to a delay that needs to be properly considered.

Further, note that the EHPO is self-supplied since it does not need an external supply, but it draws the energy for its operation directly from the RPVEH. As shown in Figure 4, the op-amp and the comparator are supplied by the capacitors C_{DC}. They are charged at the voltage levels V_p and V_n, with the energy drawn directly from the RPVEH, by the diodes that are in parallel to the MOS switches. The voltage levels V_p and V_n are nearly equal to the peak values of the input voltage v_{AB}, so that the difference $V_p - V_n$ is nearly equal to the peak-to-peak amplitude of $v_{AB}(t)$. In the experimental tests that are shown in Section 4, the average power P_{EHPO} that is drawn by the EHPO during its operation is reported for different operating conditions.

Finally, let us underline that the feedback loop implemented by the EHPO is stable as the initial start-up transient, reported in Figure 5, shows. In Figure 5, simulated waveforms are reported for an EHPO connected between a piezoelectric harvester driven by a sinusoidal acceleration and a bridge rectifier.

Table 1. Parameters of EHPO under test.

Component	Value	Component	Value
L	100 mH	R_{dt}	30 kΩ
C_{DC}	100 µF	C_{dt}	10 pF
R_m	20 Ω	NMOS	ZVN4424A
C_x	1 nF	PMOS	ZVP4424A
R_x	180 kΩ	Diodes	1N4148
R_y	15 kΩ	OP-AMP	MCP6241
R_f	100 kΩ	Comparator	LTC1440
C_b	100 nF	ΔV_H	20 mV

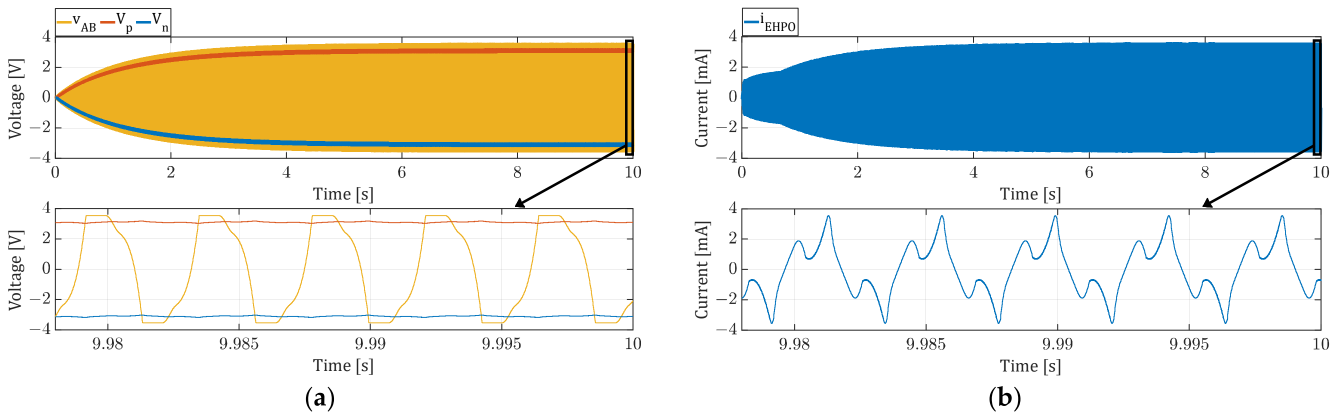

Figure 5. Simulated waveforms of EHPO (implemented with the parameters in Table 1) during the start-up transient. (**a**) Voltage waveforms; (**b**) Current waveform.

3.2. The Duty Cycle and the Switching Frequency

Differently from a PWM control, in a hysteretic control, both the duty cycle and the switching frequency change, during the circuit operation, as a function of the input voltage v_{AB}. For a proper design of the circuit, the dependence of the duty cycle and the switching frequency on v_{AB} and the circuit parameters is discussed in this section.

By imposing the quasi-stationary condition on the inductor current in Figure 4, it is possible to obtain the expression of the duty cycle $\delta(t)$. When $i_{EHPO} > 0$, the quasi-stationary condition leads to $\Delta i_{EHPO}^{NMOS\_ON} = -\Delta i_{EHPO}^{NMOS\_OFF}$, that is

$$T_{NMOS\_ON} \cdot (v_{AB} - V_n) = -T_{NMOS\_OFF} \cdot (v_{AB} - V_p), \tag{6}$$

and, hence

$$\delta_{i_{EHPO}>0} = \frac{T_{NMOS\_ON}}{T_{NMOS\_ON} + T_{NMOS\_OFF}} = \frac{V_p - v_{AB}}{V_p - V_n}. \tag{7}$$

On the other hand, when $i_{EHPO} < 0$, the quasi-stationary condition leads to $\Delta i_{EHPO}^{PMOS\_ON} = -\Delta i_{EHPO}^{PMOS\_OFF}$, that is

$$T_{PMOS\_ON} \cdot (v_{AB} - V_p) = -T_{PMOS\_OFF} \cdot (v_{AB} - V_n), \tag{8}$$

and, hence

$$\delta_{i_{EHPO}<0} = \frac{T_{PMOS\_OFF}}{T_{PMOS\_ON} + T_{PMOS\_OFF}} = \frac{V_p - v_{AB}}{V_p - V_n}. \tag{9}$$

Expressions (7) and (9) state that, under the quasi-stationary condition, the expression of the duty cycle is the same for $i_{EHPO} > 0$ and $i_{EHPO} < 0$. Therefore, under the reasonable assumption of zero mean input voltage i.e., $V_n = -V_p$, it is

$$\delta(t) = \frac{1}{2} \cdot \left[1 - \frac{v_{AB}(t)}{V_p}\right]. \tag{10}$$

To calculate the expression of the switching frequency $f_{sw}(t)$, let us consider the time evolutions of the reference current signal $i_{ref}(t)$ and of the EHPO input current $i_{EHPO}(t)$, shown in Figure 6. Since the comparator input v_e is kept within a hysteresis band ΔV_H around zero, according to Equation (2), the input current $i_{EHPO}(t)$ is kept within a hysteresis bandwidth ΔI_H equal to $R_y \cdot \Delta V_H / \left(R_f \cdot R_m\right)$ around the reference current $i_{REF}(t)$. According to the schematic in Figure 4, when $i_{EHPO}(t) > 0$ and the NMOS control signal S_n is on, the time needed by the current $i_{EHPO}(t)$ to cross, during its rise, the entire current hysteresis bandwidth ΔI_H is given by

$$t_N = \frac{L \cdot \Delta I_H}{v_{AB} - V_n} = \frac{L \cdot R_y \cdot \Delta V_H}{R_f \cdot R_m \cdot (v_{AB} - V_n)}. \tag{11}$$

Instead, when the NMOS is off, such a time is

$$t_P = \frac{L \cdot \Delta I_H}{V_p - v_{AB}} = \frac{L \cdot R_y \cdot \Delta V_H}{R_f \cdot R_m \cdot (V_p - v_{AB})}. \tag{12}$$

Moreover, it should be considered that the turn-on of the NMOS device is delayed, with respect to the end of the previous time interval t_P, by a time $t_{on} = t_{cd}$ due to the comparator delay. During t_{on}, the falling current i_{EHPO} goes out of the current hysteresis bandwidth ΔI_H of a quantity Δi_{out1} equal to

$$\Delta i_{out1} = \frac{t_{on} \cdot (V_p - v_{AB})}{L}. \tag{13}$$

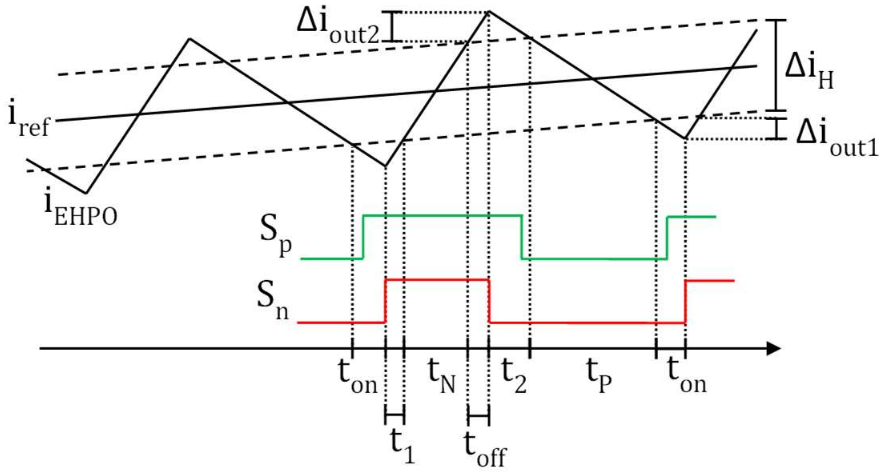

Figure 6. Typical waveforms of the MOS control signals S_p and S_n and of the currents i_{ref} and i_{EHPO}.

This implies that, after the turn-on of the NMOS, $i_{EHPO}(t)$ requires a supplementary time t_1 to come back inside the hysteresis bandwidth. t_1 is given by

$$t_1 = \frac{L \cdot \Delta i_{out1}}{v_{AB} - V_n} = \frac{V_p - v_{AB}}{v_{AB} - V_n} t_{cd}. \tag{14}$$

In a similar way, the turn-off of the NMOS device is delayed with respect to t_N by a time $t_{off} = t_{cd}$. During t_{off}, the rising current i_{EHPO} goes out of the hysteresis bandwidth ΔI_H of a quantity Δi_{out2} equal to

$$\Delta i_{out2} = \frac{t_{off} \cdot (v_{AB} - V_n)}{L}, \tag{15}$$

and the supplementary time t_2 required to come back inside the hysteresis bandwidth is equal to

$$t_2 = \frac{L \cdot \Delta i_{out2}}{V_p - v_{AB}} = \frac{v_{AB} - V_n}{V_p - v_{AB}} t_{cd}. \tag{16}$$

Taking into account that similar considerations also hold for $i_{EHPO}(t) < 0$, the total switching time T_{sw} can be expressed as the sum of the above partial times given by Equations (11), (12), (14) and (16) as

$$\begin{aligned} T_{sw} = & \tfrac{L \cdot R_y \cdot \Delta V_H}{R_f \cdot R_m \cdot (v_{AB} - V_n)} + t_{cd} + \tfrac{V_p - v_{AB}}{v_{AB} - V_n} t_{cd} + \\ & + \tfrac{L \cdot R_y \cdot \Delta V_H}{R_f \cdot R_m \cdot (V_p - v_{AB})} + t_{cd} + \tfrac{v_{AB} - V_n}{V_p - v_{AB}} t_{cd}. \end{aligned} \tag{17}$$

Thus, under the reasonable assumption of zero mean input voltage i.e., $V_n = -V_p$, the switching frequency f_{sw} is given by

$$f_{sw} = T_{sw}^{-1} = \left[\frac{2V_p^2}{V_p^2 - v_{AB}^2} \left(\frac{L \cdot R_y \cdot \Delta V_H}{R_f \cdot R_m \cdot V_p} + 2t_{cd} \right) \right]^{-1}. \tag{18}$$

Equations (10) and (18) allow us to predict the time evolution of the duty cycle and the switching frequency as a function of the input electrical quantities.

In Figure 7, Equations (10) and (18) are compared with the corresponding waveforms obtained by means of numerical simulations of the circuit in Figure 4 in case of a purely sinusoidal voltage v_{AB}. It is interesting to observe that the switching frequency varies between zero and its maximum value, with a frequency double that of v_{AB}. The maximum switching frequency is reached when the input voltage crosses zero. Moreover, it is interesting to note that when the current crosses zero, the duty cycle assumes a value equal to 0 or 1. This means that, when the current crosses zero, the switching does not take place. This behavior is confirmed by the experimental results reported in the following section.

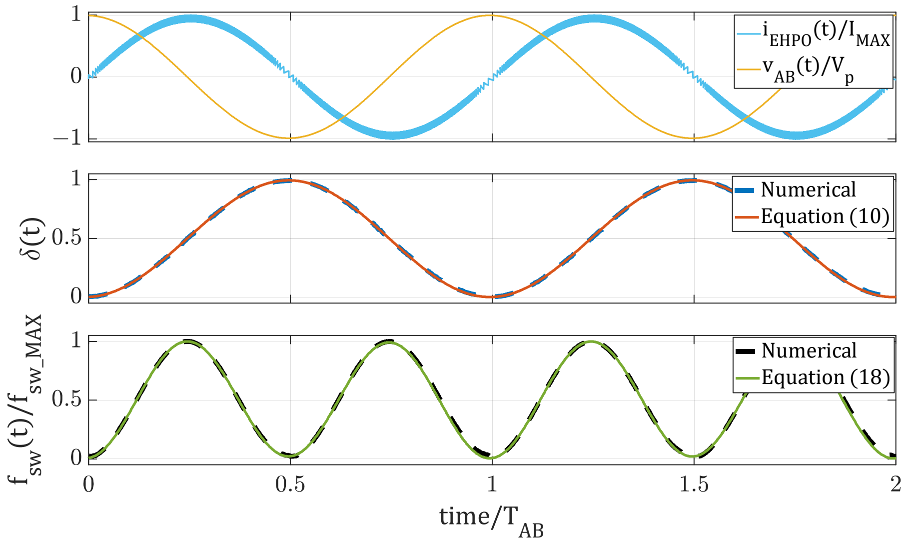

Figure 7. Waveforms as a function of the normalized time. I_{MAX} is the maximum of the current i_{EHPO} and T_{AB} is the period of v_{AB}.

From Equation (18), it is possible to predict that the maximum switching frequency is

$$f_{sw\_MAX} = \frac{1}{2} \cdot \left(\frac{L \cdot R_y \cdot \Delta V_H}{R_f \cdot R_m \cdot V_p} + 2t_{cd} \right)^{-1}. \tag{19}$$

Equation (19) provides a useful relationship between the circuit parameters and the maximum switching frequency. It is worth noting that the maximum switching frequency must be kept sufficiently low to reduce the switching losses. Therefore, the EHPO parameters should be accurately chosen to guarantee a suitable compromise between the increase in the extracted power, due to the negative capacitance emulation, and the associated switching losses.

4. Experimental Results

A prototype of the EHPO, shown in Figure 8a, was implemented with the parameters in Table 1, which ensure a compromise between negative capacitance emulation and switching loss minimization. Experimental tests were performed to show the significant increase in power extraction obtained by inserting the EHPO in parallel with a RPVEH loaded by a bridge rectifier. The tests were carried out using the architecture shown in Figure 8b and by applying both sinusoidal and non-sinusoidal vibrations to the harvester. It is worth noting that the operation of the EHPO is independent of the type of diode rectifier that is connected to the RPVEH terminals. In the considered architecture, without any loss of generality, a diode half-bridge rectifier was used, which could be useful for increasing the output DC voltage. The half-bridge rectifier shown in Figure 8b is made up of two diodes, 1N5817 by ST Microelectronics, and two 100 µF 50 V aluminum electrolytic capacitors by Lelon; the value of the resistance R_0 at the output of the bridge rectifier was varied to identify the maximum power extraction condition.

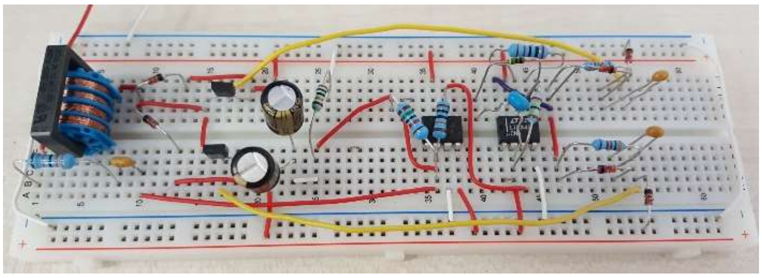

(a)

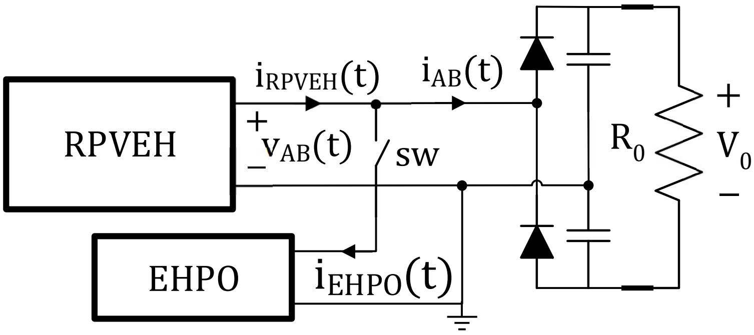

(b)

Figure 8. (**a**) Photo of the prototype of EHPO. (**b**) Architecture of the system under test.

The experimental tests were performed using the RPVEH PPA4011 by MIDE mounted on the two different mechanical configurations shown in Figure 9. The circuit parameters of the EHPO were not modified during the tests, independently of the shape of the input vibrations and the RPVEH resonance frequency resulting from its mechanical configuration. To achieve the desired acceleration, the shaker 50009 by TIRAvib equipped with the power amplifier BAA 60 was used. The accelerometers used to monitor the acceleration on the constrained terminal of the cantilever beam were the 355B04 by PCB Piezotronics (sensitivity 1 V/g and measurement range ±5 g peak) and the 352C33 by PCB Piezotronics (sensitivity 100 mV/g and measurement range ±50 g peak).

(a)

(b)

Figure 9. Harvester PPA4011 by MIDE mounted on the two tested configurations. (**a**) Configuration C1 (tuned at 232 Hz). (**b**) Configuration C2 (tuned at 477 Hz).

4.1. Sinusoidal Input Vibrations

The first tests were carried out using the RPVEH mounted on the configuration C1 shown in Figure 9a. The harvester was forced by a sinusoidal vibration with a frequency equal to the RPVEH open circuit resonance frequency, 232 Hz, and an acceleration amplitude equal to 2 g. The results of the tests are reported in Figure 10, and examples of the measured waveforms are reported in the oscilloscope screenshots in Figure 11. The meanings of the symbols are as follows: R_0 is the resistance at the output of the bridge rectifier. $P_{RPVEH\_w/EHPO}$ is the average $\langle v_{AB} \cdot i_{RPVEH} \rangle$ of the power extracted from the RPVEH when the EHPO is connected at the harvester terminals (the switch sw of Figure 8b is closed). P_{EHPO} is the average $\langle v_{AB} \cdot i_{EHPO} \rangle$ of the power that is drawn by the EHPO when it is working. $P_{DBR\_w/EHPO}$ is the average $\langle v_{AB} \cdot i_{AB} \rangle$ of the power provided to the diode bridge rectifier (DBR) when the EHPO is connected at the harvester terminals (the switch sw of Figure 8b is closed). $P_{DBR\_w/oEHPO}$ is the average $\langle v_{AB} \cdot i_{RPVEH} \rangle \equiv \langle v_{AB} \cdot i_{AB} \rangle$ of the power provided to the bridge rectifier when the EHPO is not connected (the switch sw of Figure 8b is open). In Figure 10a, the performance of the EHPO circuit is analyzed in detail by showing the total extracted power $P_{RPVEH\_w/EHPO}$, the dissipated power P_{EHPO}, and the net extracted power $P_{DBR\_w/EHPO}$. It is worth noting that, the power P_{EHPO}, which is needed for the operation of the EHPO, is directly drawn from the RPVEH terminals without any other external supply, making it a self-supplied device. In Figure 10b, the EHPO is compared with a standard DBR ($P_{DBR\_w/oEHPO}$) by considering both the total power that can be extracted from the RPVEH ($P_{RPVEH\_w/EHPO}$) and the net extracted power ($P_{DBR\_w/oEHPO}$). In Figure 10c, the percentage gains of power are shown. In particular, γ_{RPVEH} is the percentage gain of total power at the RPVEH terminals, and it is given by

$$\gamma_{RPVEH} = \frac{P_{RPVEH\_w/EHPO}}{P_{DBR\_w/oEHPO}} \cdot 100\%. \tag{20}$$

γ_{DBR} is the percentage gain of net power at the RPVEH terminals, and it is given by

$$\gamma_{DBR} = \frac{P_{DBR\_w/EHPO}}{P_{DBR\_w/oEHPO}} \cdot 100\%. \tag{21}$$

The results in Figure 10 show that, in the presence of the EHPO, a significant increase in the extracted power can be obtained, with a percentage total power gain (γ_{RPVEH}) that can reach 250% and a percentage net power gain (γ_{DBR}) that can reach about 190%.

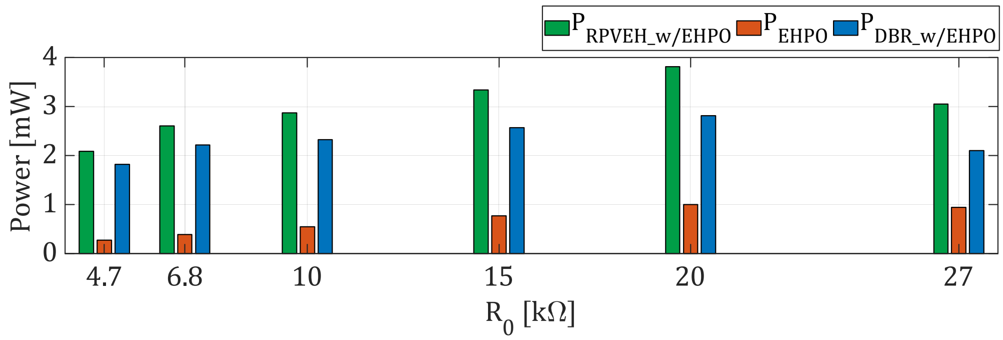

(**a**)

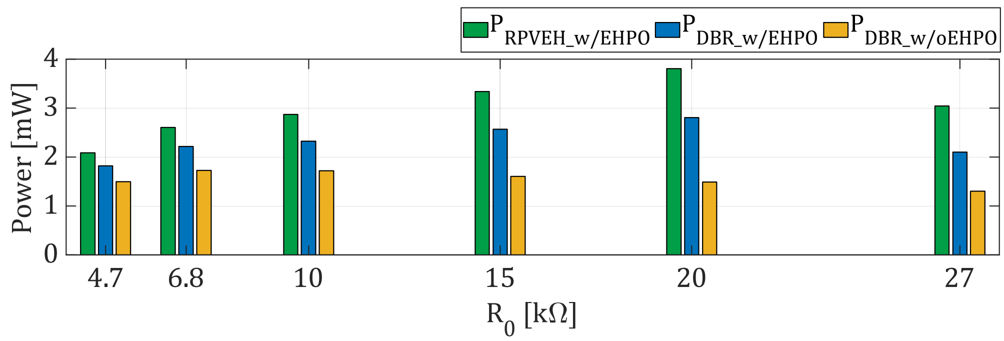

(**b**)

Figure 10. *Cont.*

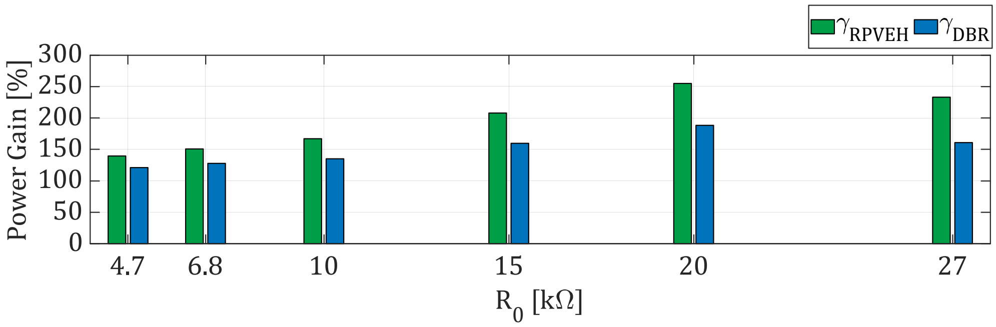

(**c**)

Figure 10. Results of the tests of configuration C1 with a sinusoidal vibration. (**a**) Performance of the EHPO circuit; (**b**) Comparison of the EHPO with a standard DBR; (**c**) Percentage gains of power. R_0 is the resistance at the output of the bridge rectifier. $P_{RPVEH\_w/EHPO}$ is the average $\langle v_{AB} \cdot i_{RPVEH} \rangle$ of the power extracted from the RPVEH when the EHPO is connected at the harvester terminals (the switch sw of Figure 8b is closed). P_{EHPO} is the average $\langle v_{AB} \cdot i_{EHPO} \rangle$ of the power that is drawn by the EHPO when it is working. $P_{DBR\_w/EHPO}$ is the average $\langle v_{AB} \cdot i_{AB} \rangle$ of the power provided to the DBR when the EHPO is connected at the harvester terminals (the switch sw of Figure 8b is closed). $P_{DBR\_w/oEHPO}$ is the average $\langle v_{AB} \cdot i_{RPVEH} \rangle \equiv \langle v_{AB} \cdot i_{AB} \rangle$ of the power provided to the bridge rectifier when the EHPO is not connected (the switch sw of Figure 8b is open). γ_{RPVEH} is the percentage gain of total power at the RPVEH terminals, and it is given by Equation (20). γ_{DBR} is the percentage gain of net power at the RPVEH terminals, and it is given by Equation (21).

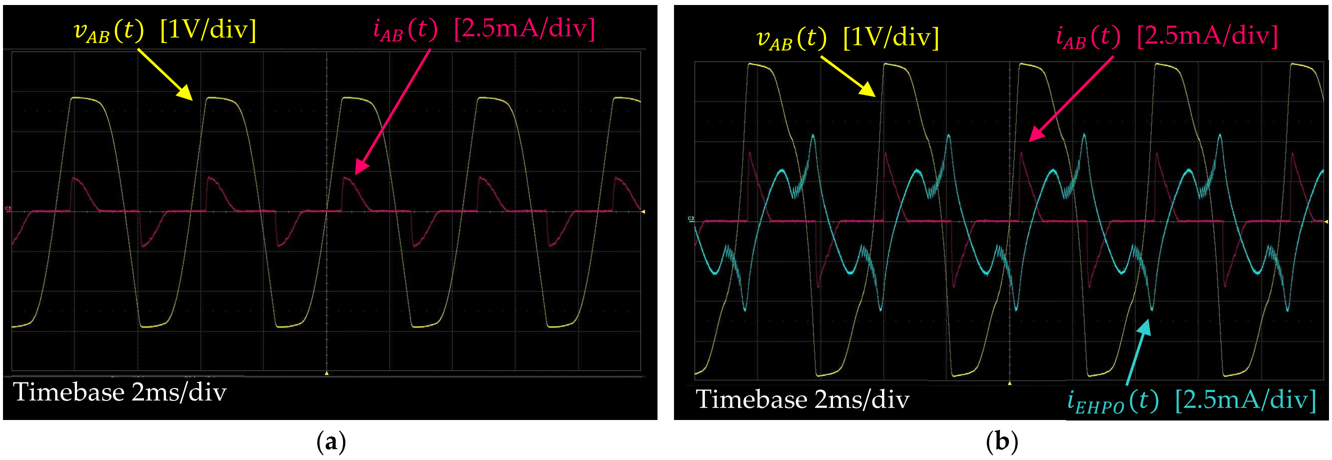

Figure 11. Waveforms measured when the harvester is tuned at 232 Hz, the acceleration is sinusoidal, and $R_0 = 20$ kΩ. (**a**) EHPO is not connected. (**b**) EHPO is connected.

The difference between γ_{RPVEH} and γ_{DBR} is due to the losses taking place in the actual implementation with discrete components of the EHPO circuit. Such losses, which are shown in detail in Figure 10a, can be reduced if an integrated implementation of the circuit is considered, leading to an increase in the net power gain (γ_{DBR}) that will approach the total power gain (γ_{RPVEH}). It is also interesting to observe that, without the EHPO, the maximum average power $P_{DBR\_w/oEHPO-MAX}$ that the standard diode bridge rectifier can extract is obtained in correspondence of $R_0 = 6.8$ kΩ and it is equal to $P_{DBR\_w/oEHPO-MAX} = 1.73$ mW, as shown in Figure 10b. On the other hand, in the presence of the EHPO, the maximum average net power is extracted in correspondence of $R_0 = 20$ kΩ and it is equal to $P_{DBR\_w/EHPO-MAX} = 2.81$ mW. This means that, by employing a DC/DC converter equipped with a Maximum Power Point Tracking (MPPT) controller [7], connected at the output of the passive bridge rectifier (both with and without EHPO), the MPPT power gain is $\gamma_{MPPT} = 100\% \cdot P_{DBR\_w/EHPO-MAX} / P_{DBR\_w/oEHPO-MAX} = 162.4\%$.

Note that the EHPO is self-supplied through the RPVEH terminals. Thus, only if v_{AB} is greater than a given threshold (related to the minimum supply voltage of the electronic components) can the EHPO work properly. In the present implementation, the minimum value needed for the peak-to-peak amplitude of v_{AB} is about 2 V.

A last interesting consideration concerns the impact of the EHPO on the operation and efficiency of the diode bridge rectifier connected at the RPVEH terminals. The comparison of the gains of power obtained at the AC side and the DC side of the rectifier as a function of the load resistance R_0 is shown in Figure 12. γ_{DC} is the percentage gain of net power at the DC side of the rectifier, and it is given by

$$\gamma_{DC} = \frac{P_{DC\_w/EHPO}}{P_{DC\_w/oEHPO}} \cdot 100\%. \tag{22}$$

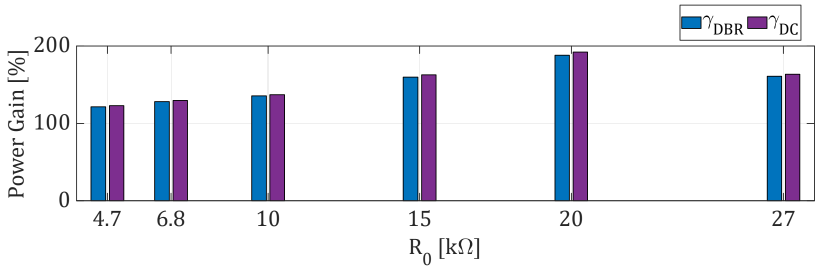

Figure 12. Results of the tests of configuration C1 with a sinusoidal vibration. R_0 is the resistance at the output of the bridge rectifier. γ_{DBR} is the percentage gain of net power at the rectifier AC side, and it is given by Equation (21). γ_{DC} is the percentage gain of net power at the rectifier DC side, and it is given by Equation (22).

$P_{DC\_w/EHPO}$ is the average $\langle (V_0^+ - V_0^-) \cdot i_{DC} \rangle$ of the power provided to the load resistance R_0 when the EHPO is connected at the harvester terminals (the switch sw of Figure 8b is closed). $P_{DC\_w/oEHPO}$ is the same average power provided to R_0 when the EHPO is not connected (the switch sw of Figure 8b is open). V_0^+ and V_0^-, respectively, are the voltage potentials, with respect to the ground, of the upper and lower terminals of R_0, and i_{DC} is the current flowing into such a resistance. In Figure 13, an example of waveforms at the AC and DC sides of the rectifier is reported with reference to the case $R_0 = 20$ kΩ. The results in Figure 12 show that the efficiency of the rectifier is essentially not affected by the connection of the EHPO, and the significant increase in the extracted power obtained in the presence of the EHPO is also confirmed at the rectifier DC side.

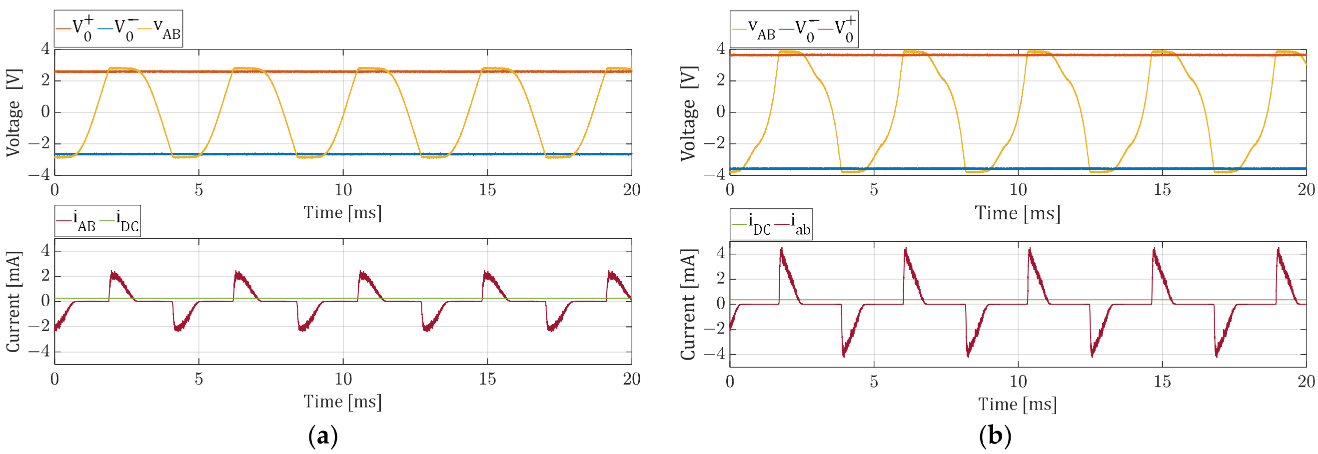

Figure 13. Example of waveforms at the AC side (v_{AB} and i_{AB}) and at the DC side (V_0^+, V_0^-, and i_{DC}, being $V_0^+ - V_0^- = V_0$) of the bridge rectifier (the harvester is tuned at 232 Hz, the acceleration is sinusoidal, and $R_0 = 20$ kΩ). (**a**) EHPO is not connected. (**b**) EHPO is connected.

4.2. Non-Sinusoidal Input Vibrations

The second set of tests of the EHPO was carried out under non-sinusoidal vibrations. Firstly, the RPVEH mounted on the configuration C1 shown in Figure 9a was used. The voltage signal that was applied to the shaker amplifier is a scaled form of the acceleration of the vibration measured on an aircraft (the fuselage side of a flying Boeing 737 [30]) and is reported in Figure 14. It is characterized by a dominant frequency around 232 Hz and produces an acceleration on the constrained terminal of the RPVEH cantilever beam with an RMS value equal to about 5 g. The results of such tests are reported in Figure 15, and examples of measured waveforms are reported in the oscilloscope screenshots in Figure 16. Figure 15 shows very good performance of the EHPO also under non-sinusoidal vibrations, with a percent total power gain (γ_{RPVEH}) that reaches about 270% and a percent net power gain (γ_{DBR}) that reaches about 180%. Moreover, by comparing the maximum net power extracted from the RPVEH when the EHPO is not connected ($P_{DBR\_w/oEHPO-MAX} = 1.1$ mW) and the maximum net power extracted when the EHPO is connected ($P_{DBR\_w/EHPO-MAX} = 1.74$ mW), it can be observed that the MPPT power gain is about $\gamma_{MPPT} = 158\%$.

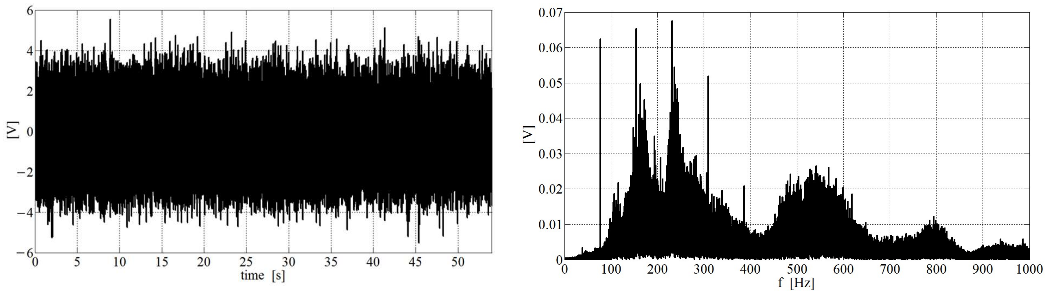

(**a**) (**b**)

Figure 14. (**a**) Voltage signal applied to the shaker amplifier (scaled form of the acceleration of the vibration measured on the fuselage side of a flying Boeing 737 [30]). (**b**) Corresponding FFT (amplitudes).

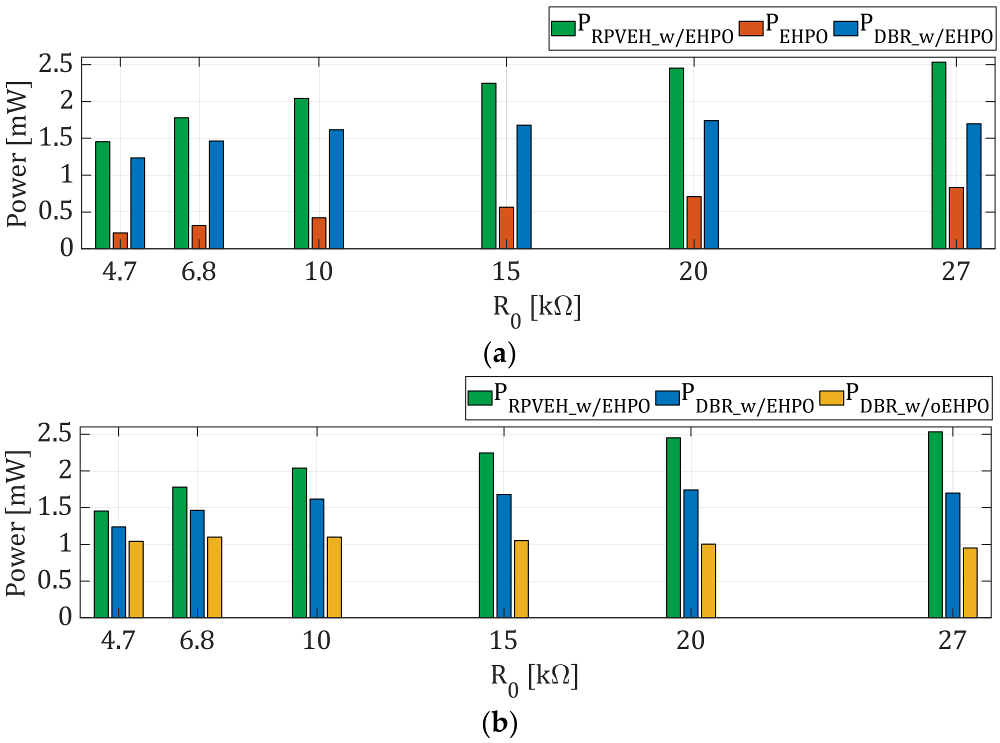

Figure 15. *Cont.*

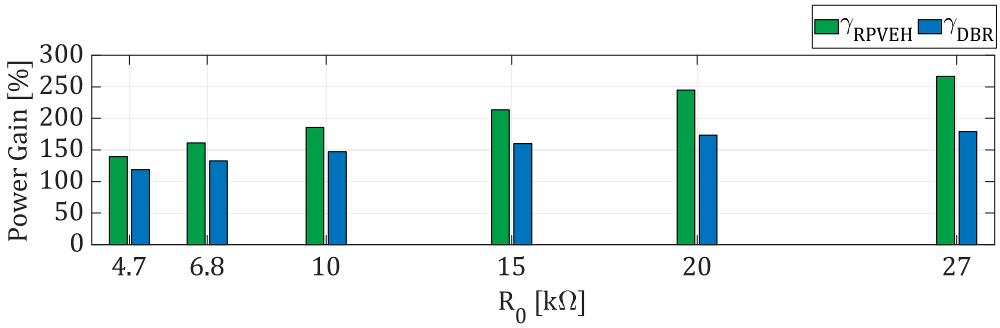

(**c**)

Figure 15. Results of the tests of configuration C1 with a non-sinusoidal vibration (signal of Figure 14). (**a**) Performance of the EHPO circuit; (**b**) Comparison of the EHPO with a standard DBR; (**c**) Percentage gains of power. $P_{RPVEH\_w/EHPO}$ is the average $\langle v_{AB} \cdot i_{RPVEH} \rangle$ of the power extracted from the RPVEH when the EHPO is connected at the harvester terminals (the switch sw of Figure 8b is closed). P_{EHPO} is the average $\langle v_{AB} \cdot i_{EHPO} \rangle$ of the power that is drawn by the EHPO when it is working. $P_{DBR\_w/EHPO}$ is the average $\langle v_{AB} \cdot i_{AB} \rangle$ of the power provided to the DBR when the EHPO is connected at the harvester terminals (the switch sw of Figure 8b is closed). $P_{DBR\_w/oEHPO}$ is the average $\langle v_{AB} \cdot i_{RPVEH} \rangle \equiv \langle v_{AB} \cdot i_{AB} \rangle$ of the power provided to the bridge rectifier when the EHPO is not connected (the switch sw of Figure 8b is open). γ_{RPVEH} is the percentage gain of total power at the RPVEH terminals, and it is given by Equation (20). γ_{DBR} is the percentage gain of net power at the RPVEH terminals, and it is given by Equation (21).

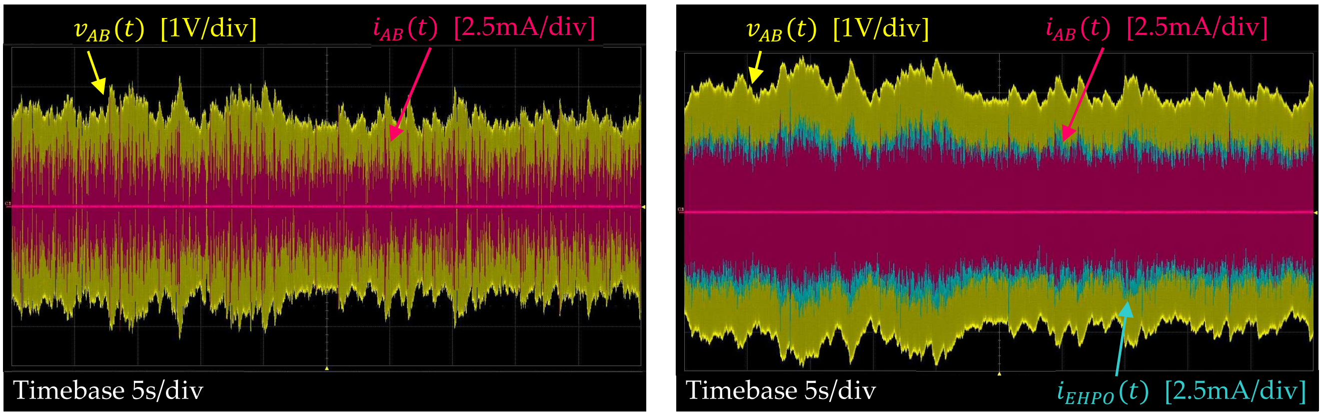

(**a**) (**b**)

Figure 16. Waveforms measured when the harvester is tuned at 232 Hz, the acceleration is non-sinusoidal, and $R_0 = 20$ kΩ. (**a**) EHPO is not connected. (**b**) EHPO is connected.

To show the ability of the EHPO to work whatever the RPVEH mechanical configuration, the harvester PPA 4011 was mounted on a different configuration i.e., C2 in Figure 9b. In such a configuration, it exhibits an open circuit resonance frequency equal to 477 Hz. Tests of such a new mechanical configuration were carried out by applying a signal to the shaker amplifier that is a scaled form of the acceleration of the vibration measured on a car (Ford Focus diesel engine turned on [31]) and reported in Figure 17. Such a vibration is characterized by a dominant frequency around 477 Hz and an RMS value of the acceleration measured on the constrained terminal of the RPVEH cantilever equal to about 5 g. It is worth noting that the same EHPO circuit, used in the previous tests with configuration C1, was also able to work with the configuration C2 without any modification.

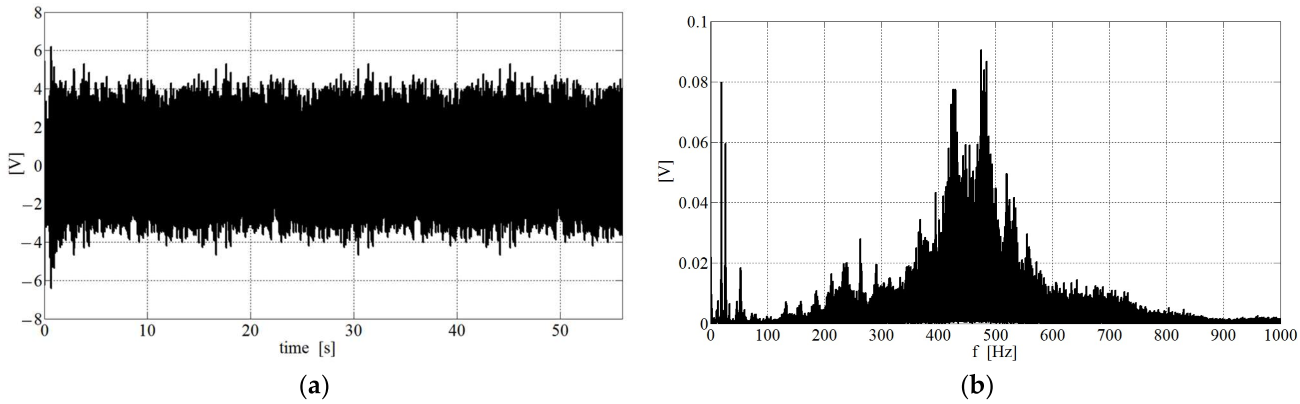

Figure 17. (**a**) Voltage signal applied to the shaker amplifier (scaled form of the acceleration of the vibration measured on a Ford Focus diesel engine turned on [31]). (**b**) Corresponding FFT (amplitudes).

The results of such experimental tests are reported in Figure 18, and examples of the measured waveforms are reported in the oscilloscope screenshots in Figure 19. The results of Figure 18 show that, also in these different mechanical conditions, the performances of the EHPO under non-sinusoidal vibrations are very good. The percentage total power gain (γ_{RPVEH}) reaches about 398%, and the percentage net power gain (γ_{DBR}) reaches about 245%. Moreover, since the maximum power extracted by the harvester without the EHPO is $P_{DBR\_w/oEHPO-MAX} = 0.69$ mW and the maximum net power extracted when the EHPO is connected is $P_{DBR\_w/EHPO-MAX} = 1.19$ mW, in this case it is about $\gamma_{MPPT} = 172.5\%$.

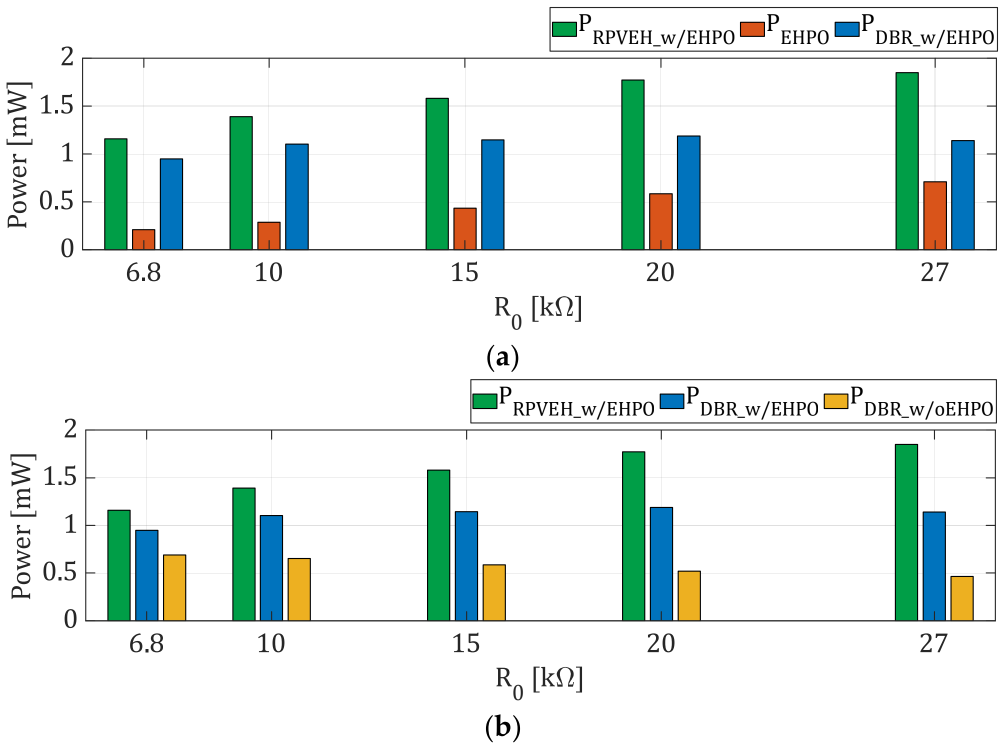

Figure 18. *Cont.*

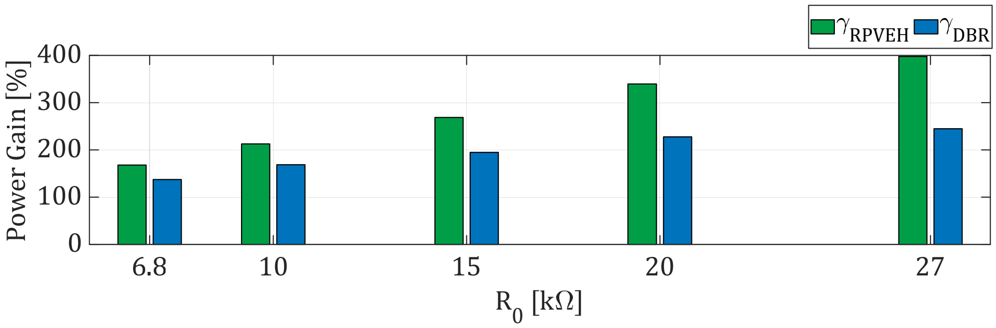

(**c**)

Figure 18. Results of the tests of configuration C2 with a non-sinusoidal vibration (signal of Figure 17). (**a**) Performance of the EHPO circuit; (**b**) Comparison of the EHPO with a standard DBR; (**c**) Percentage gains of power. $P_{RPVEH\_w/EHPO}$ is the average $\langle v_{AB} \cdot i_{RPVEH} \rangle$ of the power extracted from the RPVEH when the EHPO is connected at the harvester terminals (the switch sw of Figure 8b is closed). P_{EHPO} is the average $\langle v_{AB} \cdot i_{EHPO} \rangle$ of the power that is drawn by the EHPO when it is working. $P_{DBR\_w/EHPO}$ is the average $\langle v_{AB} \cdot i_{AB} \rangle$ of the power provided to the DBR when the EHPO is connected at the harvester terminals (the switch sw of Figure 8b is closed). $P_{DBR\_w/oEHPO}$ is the average $\langle v_{AB} \cdot i_{RPVEH} \rangle \equiv \langle v_{AB} \cdot i_{AB} \rangle$ of the power provided to the bridge rectifier when the EHPO is not connected (the switch sw of Figure 8b is open). γ_{RPVEH} is the percentage gain of total power at the RPVEH terminals, and it is given by Equation (20). γ_{DBR} is the percentage gain of net power at the RPVEH terminals, and it is given by Equation (21).

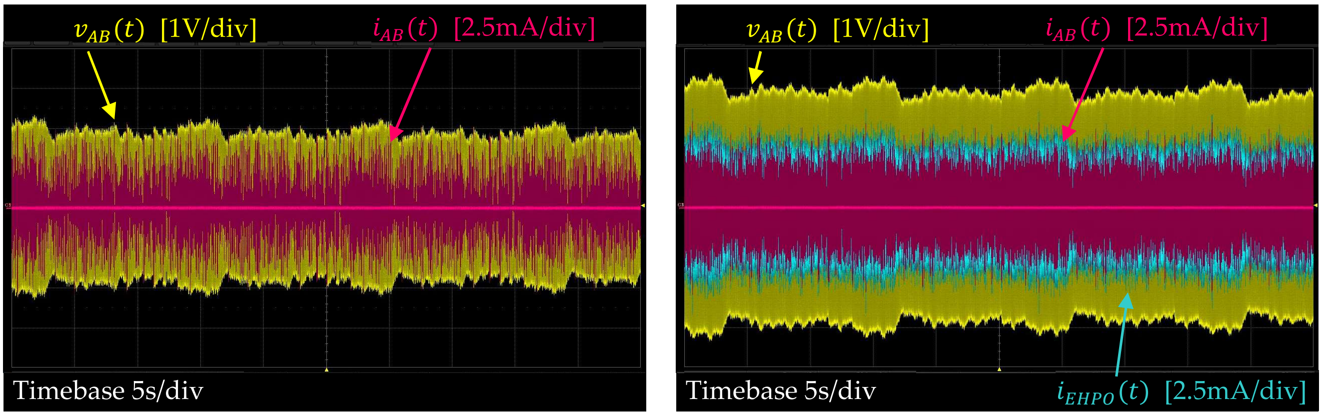

(**a**) (**b**)

Figure 19. Waveforms measured when the harvester is tuned at 477 Hz, the acceleration is non-sinusoidal, and $R_0 = 27$ kΩ. (**a**) EHPO is not connected. (**b**) EHPO is connected.

The experimental results, which have been shown in this section, confirm the ability of the EHPO to significantly increase the power extracted from an RPVEH. It is possible to highlight that the EHPO can operate both in the case of sinusoidal and non-sinusoidal vibrations, regardless of the shape of the input acceleration and the RPVEH resonance frequency. Moreover, the EHPO does not need an external power supply, but it draws the power for its operation directly from the RPVEH terminals. Such a power, P_{EHPO}, was measured in all the different testing conditions and reported in Figures 10a, 15a and 18a. P_{EHPO}, which is the reason for the difference between γ_{DBR} and γ_{RPVEH}, can be strongly reduced with an integrated implementation of the EHPO.

A comparison of the proposed EHPO circuit with the most recent RPVEH optimizer circuits is reported in Table 2. In the last few years, many self-supplied circuits have been proposed implementing SSHI, SECE, and Impedance Matching techniques. They are mainly devoted to increasing the extracted power from RPVEHs by compensating the output piezo capacitance. The proposed EHPO circuit is designed for the same goal, but it exploits a very light control technique aimed at emulating a negative capacitance. Moreover, research efforts on non-sinusoidal vibrations have mainly focused on circuit optimization for impact vibrations. Differently, the EHPO, by emulating a negative capacitance, can compensate the RPVEH output capacitance in every working condition, regardless of the shape of the non-sinusoidal forcing acceleration. Furthermore, among the circuits implemented with discrete components, the EHPO is the only one that is tested both in sinusoidal and non-sinusoidal conditions, and, despite its simplicity, it leads to very high gains of power in both conditions. Finally, considering that the integrated circuit implementation allows an increase in overall efficiency, further improvements in power gain will be possible thanks to an integrated implementation of the EHPO.

Table 2. Comparison of the proposed EHPO with the state of the art.

Publication	2021 [32]	2022 [33]	2021 [34]	2022 [35]	2023 [36]	2021 [37]	2022 [38]	This Work
Type of Circuit	IM (2)	SSHI (3) and IM	SSHI and MPPT (4)	Rectifier-less SSHI	SSHI	SSHI	SECE (7)	EHPO (switch-mode converter for negative capacitance emulation)
Self-supplied	Yes	Yes	Yes	Yes (6)	Yes	Yes	Yes	Yes
Type of prototype	Discrete components	Integrated chip	Discrete components	Discrete components	Discrete components	Integrated chip	Discrete components	Discrete components
Tested RPVEH	Custom piezo device	PZT S452-J1FR-1808XB	Custom piezo device	S452-J1FR-1808XB	AB4113BLW100-R by Murata	MIDE V22BL	Piezo by Eleceram Technology	MIDE PPA-4011
Sinusoidal Vibration Characteristics	N/A	N/A	30 Hz, 4 V (5)	N/A	N/A	208 Hz, 0.13 g	N/A	232 Hz, 2 g
Maximum power under sinusoidal vibrations	N/A	N/A	237.2 µW	N/A	N/A	3.84 µW	N/A	2.81 mW
Power gain under sinusoidal vibrations (1)	N/A	N/A	292%	N/A	N/A	523%	N/A	190%
Non-sinusoidal vibration characteristics	Impact	Impact due to the rotation of air blades under a wind speed of 1.46 m/s	N/A	Impact	Footsteps pressure of a person (59 kg) walking with moderate speed	N/A	Impact	Scaled form of the vibration on a Ford Focus diesel engine turned on
Maximum power under non-sinusoidal vibrations	1.05 mW	294.2 µW	N/A	≈82 µW (6)	3.6 mW	N/A	200 µ	1.19 mW
Power gain under non-sinusoidal vibrations (1)	122%	368%	N/A	176% (6)	N/A	N/A	≈ 118% (8)	245%

(1) Percent gain with respect to a passive diode bridge rectifier. (2) IM = Impedance Matching. (3) SSHI = Synchronized Switching Harvesting on Inductor. (4) MPPT = Maximum Power Point Tracking. (5) Harvester Open Circuit Voltage. (6) Only simulation results are provided. (7) SECE = Synchronous Electric Charge Extraction. (8) Estimated from graphs in the paper.

5. Conclusions

In this paper, a new self-supplied circuit, named the EHPO, aimed at the optimization of the extraction of power from RPVEHs, was presented and discussed. It compensates the electrical current drawn by the RPVEH output capacitance by exploiting a switch-mode converter and a very light control circuit based on a hysteresis comparator. By emulating a negative capacitance, the EHPO can lead to a significant increase in the power provided by an RPVEH to a passive rectifier. A prototype of the proposed circuit was implemented using discrete components on a breadboard and tested. The experimental results show that the EHPO significantly increases the power extracted from a commercial RPVEH, both in the case of sinusoidal and non-sinusoidal vibrations, regardless of the shape of the forcing acceleration and the RPVEH resonance frequency. The EHPO's performance is very promising and can be further improved by integrating it on a chip.

6. Patents

In this paper, a new technology is presented and discussed for the first time after patent granting.

European Patent EP3942686. Title: Electronic device and method for the maximization of the average power extracted from a vibration harvester. Inventors: L. Costanzo, A. Lo Schiavo, M. Vitelli. Applicant: Università degli Studi della Campania Luigi Vanvitelli. Italian Patent Granting Date: 4 February 2021, European Patent Publication Date: 26 January 2022; Links:

https://register.epo.org/application?number=EP20719490 (accessed on 23 May 2023).

https://patentscope.wipo.int/search/en/detail.jsf?docId=EP348440005 (accessed on 23 May 2023).

https://patents.google.com/patent/EP3942686A1/en (accessed on 23 May 2023).

Author Contributions: Conceptualization, L.C., A.L.S. and M.V.; Data curation, L.C., A.L.S., and M.V.; Formal analysis, L.C., A.L.S. and M.V.; Funding acquisition, L.C., A.L.S. and M.V.; Investigation, L.C., A.L.S. and M.V.; Methodology, L.C., A.L.S. and M.V.; Project administration, L.C., A.L.S. and M.V.; Resources, L.C., A.L.S. and M.V.; Software, L.C., A.L.S. and M.V.; Validation, L.C., A.L.S. and M.V.; Visualization, L.C., A.L.S. and M.V.; Writing–original draft, L.C., A.L.S. and M.V.; Writing—review and editing, L.C., A.L.S. and M.V. All authors have read and agreed to the published version of the manuscript.

Funding: This work was supported in part by Università degli Studi della Campania Luigi Vanvitelli in the framework of "Piano Strategico di Ateneo 2021–2023-Azione strategica R1.S2" under Grant SCAVENGE.

Data Availability Statement: No Available data.

Acknowledgments: The vibration data of Section 4.2 is provided on an "as is" basis through EnABLES, funded by the EU H2020 Infrastructure Programme (H2020-INFRAIA-02-2017) under the Grant Agreement 730957.

Conflicts of Interest: The authors declare no conflict of interest.

References

1. Hung, L.-L.; Leu, F.-Y.; Tsai, K.-L.; Ko, C.-Y. Energy-Efficient Cooperative Routing Scheme for Heterogeneous Wireless Sensor Networks. *IEEE Access* **2020**, *8*, 56321–56332. [CrossRef]
2. Femine, A.D.; Gallo, D.; Landi, C.; Schiavo, A.L.; Luiso, M. Low Power Contactless Voltage Sensor for Low Voltage Power Systems. *Sensors* **2019**, *19*, 3513. [CrossRef] [PubMed]
3. Gulati, K.; Boddu, R.S.K.; Kapila, D.; Bangare, S.L.; Chandnani, N.; Saravanan, G. A review paper on wireless sensor network techniques in Internet of Things (IoT). *Mater. Today Proc.* **2021**, *51*, 161–165. [CrossRef]
4. Harb, A. Energy harvesting: State-of-the-art. *Renew. Energy* **2011**, *36*, 2641–2654. [CrossRef]
5. Costanzo, L.; Vitelli, M. Tuning Techniques for Piezoelectric and Electromagnetic Vibration Energy Harvesters. *Energies* **2020**, *13*, 527. [CrossRef]
6. Costanzo, L.; Liu, M.; Schiavo, A.L.; Vitelli, M.; Zuo, L. Backpack Energy Harvesting System with Maximum Power Point Tracking Capability. *IEEE Trans. Ind. Electron.* **2022**, *69*, 506–516. [CrossRef]
7. Brenes, A.; Morel, A.; Juillard, J.; Lefeuvre, E.; Badel, A. Maximum power point of piezoelectric energy harvesters: A review of optimality condition for electrical tuning. *Smart Mater. Struct.* **2020**, *29*, 033001. [CrossRef]
8. Costanzo, L.; Schiavo, A.L.; Vitelli, M. Active Interface for Piezoelectric Harvesters Based on Multi-Variable Maximum Power Point Tracking. *IEEE Trans. Circuits Syst. I Regul. Pap.* **2020**, *67*, 2503–2515. [CrossRef]
9. Piliposian, G.; Hasanyan, A.; Jilavyan, H. On the Sensing, Actuating and Energy Harvesting Properties of a Composite Plate with Piezoelectric Patches. *Int. J. Precis. Eng. Manuf. Technol.* **2020**, *7*, 657–668. [CrossRef]
10. Li, T.; Lee, P.S. Piezoelectric Energy Harvesting Technology: From Materials, Structures, to Applications. *Small Struct.* **2022**, *3*, 2100128. [CrossRef]
11. Brito-Pereira, R.; Ribeiro, C.; Pereira, N.; Lanceros-Mendez, S.; Martins, P. Printed multifunctional magnetically activated energy harvester with sensing capabilities. *Nano Energy* **2022**, *94*, 106885. [CrossRef]

12. Shi, Y.; Li, N.; Ye, J.; Ma, J. Enhanced magnetoelectric response in nanostructures due to flexoelectric and flexomagnetic effects. *J. Magn. Magn. Mater.* **2020**, *521*, 167523. [CrossRef]
13. Kong, C.S. A general maximum power transfer theorem. *IEEE Trans. Educ.* **1995**, *38*, 296–298. [CrossRef]
14. Liao, Y.; Liang, J. Maximum power, optimal load, and impedance analysis of piezoelectric vibration energy harvesters. *Smart Mater. Struct.* **2018**, *27*, 075053. [CrossRef]
15. Minami, M. Improvement in Output Characteristics Using a Resonator and Passive Rectifiers in Vibration Generators. *IEEE Trans. Power Electron.* **2018**, *34*, 7184–7191. [CrossRef]
16. Ulusan, H.; Gharehbaghi, K.; Zorlu, O.; Muhtaroglu, A.; Kulah, H. A Fully Integrated and Battery-Free Interface for Low-Voltage Electromagnetic Energy Harvesters. *IEEE Trans. Power Electron.* **2014**, *30*, 3712–3719. [CrossRef]
17. Hsieh, C.-Y.; Huang, B.; Golnaraghi, F.; Moallem, M. Regenerative Skyhook Control for an Electromechanical Suspension System Using a Switch-Mode Rectifier. *IEEE Trans. Veh. Technol.* **2016**, *65*, 9642–9650. [CrossRef]
18. Datasheet. Available online: https://www.analog.com/en/products/ltc3588-1.html (accessed on 23 May 2023).
19. Datasheet. Available online: https://www.analog.com/en/products/ltc3331.html (accessed on 23 May 2023).
20. Datasheet. Available online: http://www.ti.com/tool/TIDA-00690#0 (accessed on 23 May 2023).
21. Datasheet. Available online: https://datasheets.maximintegrated.com/en/ds/MAX17710.pdf (accessed on 23 May 2023).
22. Costanzo, L.; Schiavo, A.L.; Vitelli, M. Design Guidelines for the Perturb and Observe Technique for Electromagnetic Vibration Energy Harvesters Feeding Bridge Rectifiers. *IEEE Trans. Ind. Appl.* **2019**, *55*, 5089–5098. [CrossRef]
23. Guyomar, D.; Badel, A.; Lefeuvre, E.; Richard, C. Toward energy harvesting using active materials and conversion improvement by nonlinear processing. *IEEE Trans. Ultrason. Ferroelectr. Freq. Control* **2005**, *52*, 584–595. [CrossRef]
24. Wu, L.; Do, X.-D.; Lee, S.-G.; Ha, D.S. A Self-Powered and Optimal SSHI Circuit Integrated with an Active Rectifier for Piezoelectric Energy Harvesting. *IEEE Trans. Circuits Syst. I Regul. Pap.* **2017**, *64*, 537–549. [CrossRef]
25. Dicken, J.; Mitcheson, P.D.; Stoianov, I.; Yeatman, E.M. Power-extraction circuits for piezoelectric energy harvesters in miniature and low-power applications. *IEEE Trans. Power Electron.* **2012**, *27*, 4514–4529. [CrossRef]
26. Lefeuvre, E.; Badel, A.; Brenes, A.; Seok, S.; Woytasik, M.; Yoo, C.S. Analysis of piezoelectric energy harvesting system with tunable SECE interface. *Smart Mater. Struct.* **2017**, *26*, 035065. [CrossRef]
27. Patent. Available online: https://patentscope.wipo.int/search/en/detail.jsf?docId=EP348440005&_cid=P10-L2A8TC-36138-1 (accessed on 23 May 2023).
28. De Marneffe, B.; Preumont, A. Vibration damping with negative capacitance shunts: Theory and experiment. *Smart Mater. Struct.* **2008**, *17*, 035015. [CrossRef]
29. Neri, I.; Travasso, F.; Mincigrucci, R.; Vocca, H.; Orfei, F.; Gammaitoni, L. A real vibration database for kinetic energy harvesting application. *J. Intell. Mater. Syst. Struct.* **2012**, *23*, 2095–2101. [CrossRef]
30. Vibration Signal. Available online: http://realvibrations.nipslab.org/node/235 (accessed on 23 May 2023).
31. Vibration Signal. Available online: http://realvibrations.nipslab.org/node/152 (accessed on 23 May 2023).
32. Yao, M.; Li, J.; Niu, Y. Adaptive impedance matching for power management circuit for a piezoelectric energy harvester on the bridge. *Sens. Actuators A Phys.* **2021**, *331*, 112986. [CrossRef]
33. Yang, L.; Wei, T.; Chen, N. High-Efficiency Energy Management Circuit Combining Synchronized Switch Harvesting on Inductor Rectifier and Impedance Matching for Impact-Type Piezoelectric Energy Harvester. *Energy Technol.* **2022**, *10*, 2200434. [CrossRef]
34. Fang, S.; Xia, H.; Xia, Y.; Ye, Y.; Shi, G.; Wang, X.; Chen, Z. An Efficient Piezoelectric Energy Harvesting Circuit with Series-SSHI Rectifier and FNOV-MPPT Control Technique. *IEEE Trans. Ind. Electron.* **2021**, *68*, 7146–7155. [CrossRef]
35. Yang, L.; Wei, T.; Chen, N. A Piezoelectric Energy Management Circuit Combining ReL-SSHI and MPPT for Impact-Type Piezoelectric Harvesters. In Proceedings of the 2022 7th International Conference on Integrated Circuits and Microsystems (ICICM), Xi'an, China, 28–31 October 2022; pp. 12–16. [CrossRef]
36. Ammar, M.B.; Sahnoun, S.; Fakhfakh, A.; Viehweger, C.; Kanoun, O. Self-Powered Synchronized Switching Interface Circuit for Piezoelectric Footstep Energy Harvesting. *Sensors* **2023**, *23*, 1830. [CrossRef]
37. Chamanian, S.; Ciftci, B.; Muhtaroglu, A.; Kulah, H. A Self-Powered and Area Efficient SSHI Rectifier for Piezoelectric Harvesters. *IEEE Access* **2021**, *9*, 117703–117713. [CrossRef]
38. Lo, Y.; Shu, Y. Self-powered SECE piezoelectric energy harvesting induced by shock excitations for sensor supply. *Mech. Syst. Signal Process.* **2022**, *177*, 109123. [CrossRef]